

Article

Design Procedure of a Frequency Reconfigurable Metasurface Antenna at mmWave Band

Bokamoso Kebatho Ledimo , Pako Moaro , Reuben Ramogomana , Modisa Mosalaosi 
and Bokamoso Basutli 

Department of Electrical, Computer, and Telecommunications Engineering, Faculty of Engineering, Botswana International University of Science and Technology, Private Bag 16, Palapye 10071, Botswana; pako.moaro@studentmail.biust.ac.bw (P.M.); reuben.ramogomana@studentmail.biust.ac.bw (R.R.); mosalaosim@biust.ac.bw (M.M.); basutlib@biust.ac.bw (B.B.)

* Correspondence: bokamoso.ledimo@studentmail.biust.ac.bw

Abstract: The use of the millimeter wave (mmWave) spectrum and further exploration of sub-mmWave has led to a new era in wireless communication, as the need for higher data rates grows. High frequencies, on the other hand, incur a higher path loss, requiring an increase in antenna gain requirements. Metasurfaces, which emerge as a promising technology for mitigating path loss effects by utilizing two dimensional (2D) arrays of engineered meta-atoms resembling metamaterials that control the surface's electromagnetic response have been introduced. Currently, metasurfaces are primarily considered as passive reflecting devices in wireless communications, assisting conventional transceivers in shaping propagation environments. This paper presents an alternative application of metasurfaces for wireless communications as active reconfigurable antennas for next generation transceivers. A framework that demonstrates the design process of a metasurface antenna structure was introduced and further used to design a 4×4 array and its reconfigurable counterpart. In contrast to conventional phased array antennas, a reconfigurable metasurface (RMS) antenna does not require phase-shifters and amplifiers, which leads to reduced cost. Instead, each individual element achieves reconfigurability by shifting the resonating frequency using semiconductor devices such as PIN diodes. The proposed metasurface antenna is designed to operate at a frequency of 28 GHz and 40 GHz. In addition, an increase in gain and directivity was observed when diodes were added to the metasurface antenna array. However, due to PIN diodes being connected to metallic strips in the metasurface antenna array, loss can occur due to power dissipation, which results in a decrease in radiation efficiency.

Keywords: massive MIMO; reconfigurable metasurface antenna; antenna design; split ring resonators



Citation: Ledimo, B.K.; Moaro, P.; Ramogomana, R.; Mosalaosi, M.; Basutli, B. Design Procedure of a Frequency Reconfigurable Metasurface Antenna at mmWave Band. *Telecom* **2022**, *3*, 379–395. <https://doi.org/10.3390/telecom3020020>

Academic Editor: Dimitris E. Anagnostou

Received: 10 March 2022

Accepted: 20 April 2022

Published: 9 June 2022

Publisher's Note: MDPI stays neutral with regard to jurisdictional claims in published maps and institutional affiliations.



Copyright: © 2022 by the authors. Licensee MDPI, Basel, Switzerland. This article is an open access article distributed under the terms and conditions of the Creative Commons Attribution (CC BY) license (<https://creativecommons.org/licenses/by/4.0/>).

1. Introduction

The under-utilized mmWaves spectrum gave researchers an opportunity to investigate and exploit this band with the aim to curb issues on bandwidth and channel capacity associated with 5G and 6G technologies [1]. Consequently, new wireless communication technologies are emerging, including mmWaves utilization and further exploration of sub-mmWaves, as the need for higher data rates grows [2–5]. However, high frequencies introduce high path loss, which results in the need for improved hardware designs and performance such as antenna gain requirements [2]. One enabling technology is massive multiple-input multiple-output (mMIMO), which is developed to increase the throughput and spectral efficiency by deploying thousands of antennas at a base station [6,7]. In particular, mMIMO aims to have more antenna elements at the access points than the number of active user equipment in any cell at any point in time. This induces more orthogonal channels and consequently achieves high spectral efficiency. Despite these benefits of mMIMO, implementing large scale antenna arrays in practice has proven to be a challenge [8]. Among these challenges are high fabrication cost, increased power consumption,

and constrained physical size [9,10]. With significantly improved cost and manufacturing efficiency, metasurface antennas are emerging as an alternative to conventional electronic scanned antennas [8,11–14].

Metasurfaces are the 2D counterparts of metamaterials, which consist of sub-wavelength metallic or dielectric particles that are used to control or modify various parameters, such as amplitude, phase, and polarization [15–17]. In recent years, scientists have been interested in the use of artificial materials, which are envisaged to generate significant benefits and introduces various applications. Metamaterials are among these artificial materials, as they are composed of closely spaced sub-wavelength meta-atoms which resonantly couple to both the electric or magnetic components of the incident electromagnetic fields, thereby exhibiting properties that are not found in nature [18–20]. By modifying their permittivity and permeability values, metamaterials can control the propagation of a wave, but they still rely on the propagation phenomena to manipulate electromagnetic (EM) waves [21]. In addition, their 3D nature makes them challenging to fabricate and also results in relatively bulky structures as they manipulate a wave over an extremely thin layer [19,22]. Moreover, the planar structure of metasurfaces facilitates the easy fabrication and highly cost-effective fabrication process when compared to the creation of complex 3D metamaterials. Some of the shortfalls brought on by metamaterials can be addressed by the metasurface, which are less bulky. As compared to metamaterials, metasurfaces are considered to be 2D structures instead of 3D structures. As a result, these metasurface structures are used for a variety of applications, including controllable “smart” surfaces, miniaturized cavity resonators, novel wave-guiding structures, compact and wide-angle absorbers and impedance-matching surfaces.

Metamaterials and Metasurface Structures

In recent years, scientists have embarked on research regarding the use of artificial materials, which generate significant benefits and introduces various applications. Metamaterials are among these artificial materials, as they are composed of closely spaced sub-wavelength meta-atoms, which resonantly couple to both the electric or magnetic components of the incident electromagnetic fields, thereby exhibiting properties that are not found in nature, as shown in Figure 1 [18–20].

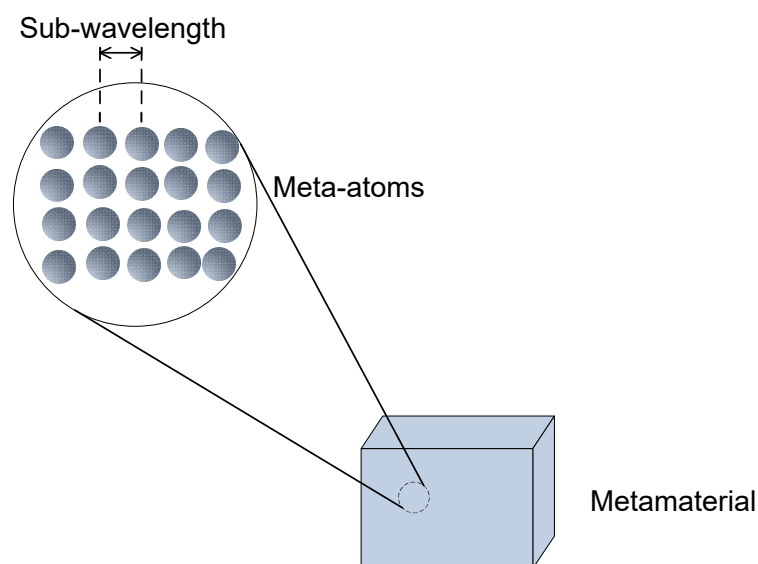


Figure 1. From meta-atoms to metamaterials.

Consequently, they have physical properties that are largely determined by their structures rather than their individual attributes. Furthermore, different structures influence the categorization of metamaterials according to their electrical permittivity and magnetic

permeability, denoted as ϵ and (μ) values, respectively [23]. The authors in [24] made it possible to classify these materials in four different classes, as shown in Figure 2.

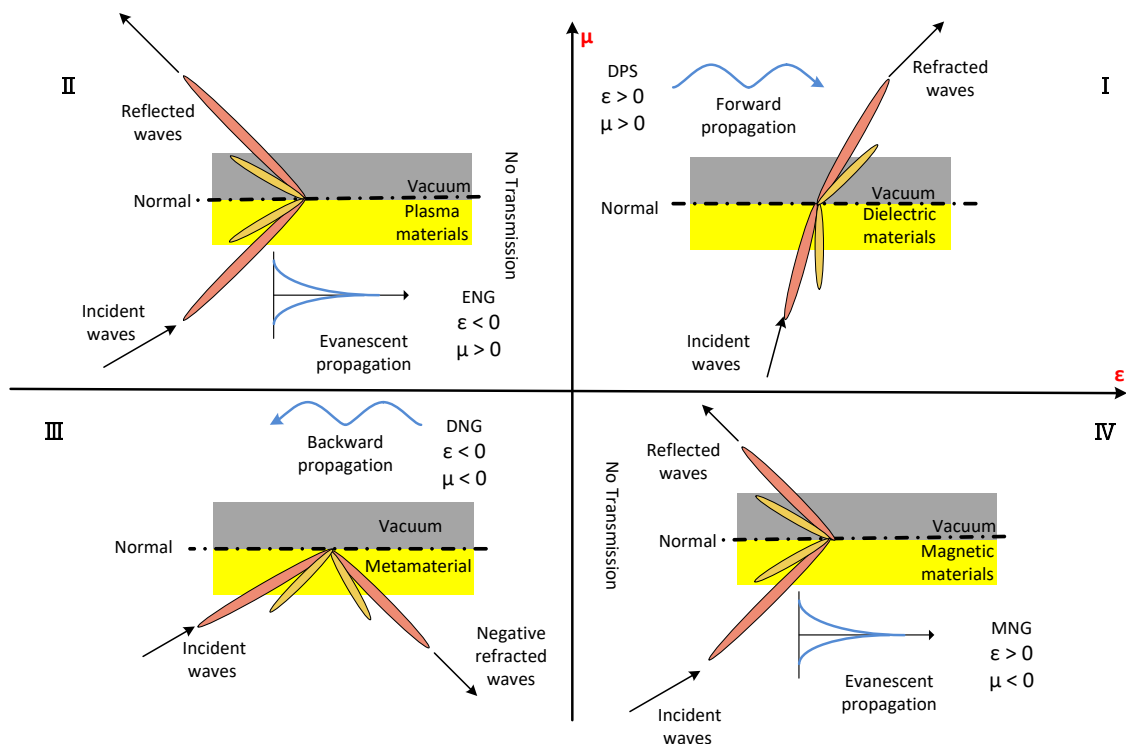


Figure 2. (I–IV) Metamaterial classifications based on permittivity and permeability values.

The first quadrant from Figure 2 is characterized by the existence of both positive ϵ and μ values. Such materials are known as double positive (DPS). These can be found in nature, for example, in dielectric materials where EM waves propagate. The second quadrant consists of materials that are represented by a plasma and are known as epsilon negative medium (ENG) due to $\epsilon < 0$ and $\mu > 0$ values [25]. The third quadrant is of interest, being that both ϵ and μ values of materials are negative and not found in nature, hence why it is called the double negative medium (DNG). Furthermore when plane waves propagate in metamaterials, the electric field, magnetic field, and wave vector adopt the left-hand rule, hence why they are referred to as left-handed materials [26]. The fourth quadrant is called the mu negative medium (MNG), represented by magnetic materials as it entails positive ϵ and negative μ values. From Figure 2, one can see that the majority of waves propagate through two mediums namely; region I and III.

Presently, most metamaterials are being designed with two basic types of structures: dense arrays of thin wires (the electric dipoles) and arrays of split-ring resonators (SRRs) (the magnetic loops), which are metallic rings etched onto a dielectric substrate in a concentric pattern [27,28]. According to the authors in [29], SRRs are considered as unit cells of DNG metamaterials. In order to attain DNG mediums, ENG and MNG mediums are combined, as shown in Figure 3. This paper will focus on the third quadrant as they give metamaterials the property/ability to control EM waves.

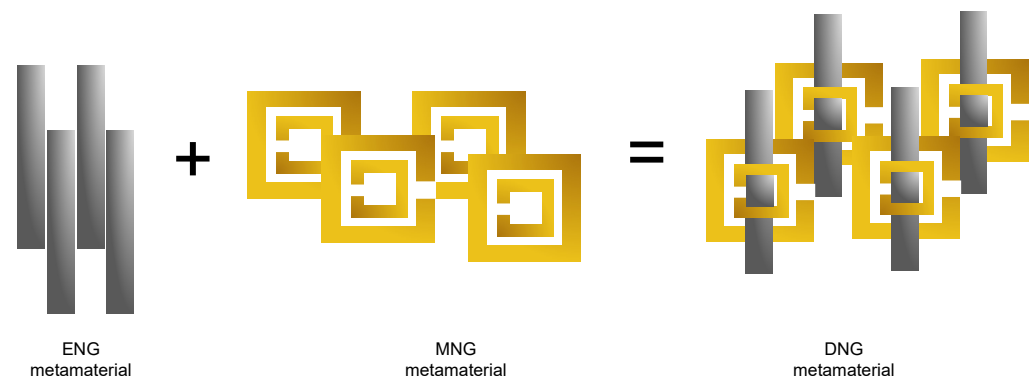


Figure 3. Creating DNG metamaterials by combining wires and SRR.

Metasurface unit cells consist of SRRs, which comprise negative effective permeability at frequencies closer to the resonant frequency and are used to make left handed media with negative refractive index [30]. The geometric parameters of the ring resonator and the resonant frequency are dependent on each other [28]. Over the course of development of metasurfaces, the limitations of fixed response metasurfaces in realistic applications, i.e., limited working bandwidths and fixed wave manipulation capabilities, were realized [31]. As a result, many efforts have been devoted to developing reconfigurable metasurfaces (RMS) that can actively control EM waves with external tunings. RMSs involve adding tunability to each unit cell which allows for more capabilities of metasurface applications. In the context of wireless communication, they are mostly considered passive reflecting devices used to shape the propagation environment [32–35]. As an alternative, recent studies presented an application of RMSs as massive MIMO active reconfigurable antennas with developed analog signal processing capabilities for next generation transceivers [8,14,36]. RMS antennas achieve higher power efficiency as they eliminate the need for active phase shifters. Furthermore, the RMS antenna elements can be packed into a relatively small space and be operated over a wide range of frequencies, making them more flexible in size than conventional antennas [14].

2. Related Works

Several researchers have reported various RMSs in the last decade [22,37–45]. Works in [42] proposed a reconfigurable metasurface antenna based on a PIN diode for beam switching applications. The authors proposed a metasurface consisting of periodic double-SRR, whose fundamental resonant frequency could easily be controlled by their respective dimensions. Based on their simulations and experiments, the proposed metasurface antenna had good impedance matching and moderate gain performance of about 6 dBi across the band of interest. In Ref. [46], the authors presented a dynamically reconfigurable holographic metasurface antenna for applications in near-field beam focusing. Through the use of the proposed metasurface antenna, the authors achieved beam-focusing without requiring phase shifters and power amplifiers. This concluded that the proposed metasurface antenna was suitable for applications that require dynamic reconfigurability, such as imaging and wireless power transfer.

Works in Refs. [43,47] presented a reconfigurable metasurface antenna that manipulated scattering fields by liquid metal. The reflected element phase responses underwent distinct phase differences when the metal shape of the metasurface element changed along the polarization direction. It was concluded that the liquid-metal metasurface antenna presented had less system complexity, lower cost, and much lower power consumption. In Ref. [48], a frequency reconfigurable dielectric resonator antenna using metasurfaces was proposed. The attained bandwidth and gain of the proposed metasurface antenna was 1.1 GHz and 7.8 dBi, respectively. The authors in Ref. [49] designed and evaluated rectangular and circular SRR structures to create a metamaterial superstructure with improved antenna characteristics such as gain, bandwidth, and radiation pattern. However,

from literature, there has not been an explicit method on how to calculate each geometrical parameter of SRRs.

Contribution

This paper proposes a unified simple design procedure used in antennas to calculate the geometrical parameters of SRRs, which are used in metasurface unit cells. The proposed unit cell is further used to design a PIN diode based elements reconfigurable metasurface antenna for the realization of dual band operation at mmWave frequencies. The main contributions of this chapter are summarized as follows:

- Firstly, a demonstration of a step-by-step procedure on how to achieve SRR geometrical parameters at dual frequency of operation is provided;
- Secondly, the proposed unit cell was used to design a 16 element frequency RMS;
- Finally, the characteristics of the proposed frequency RMS were analyzed and compared with previous works.

3. Design Procedure

According to [50], ring resonators are described as two identical half guided wavelength $\lambda_g/2$, which establish standing waves in parallel. Figure 4 depicts a schematic view of the dual band square SRR structure.

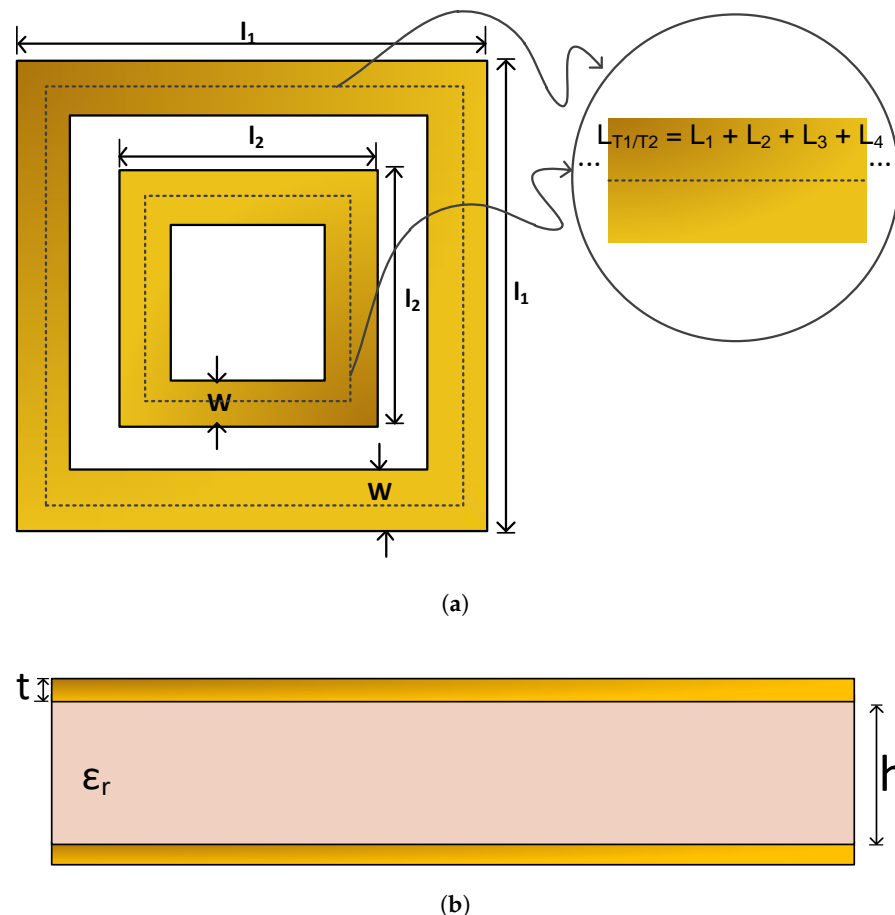


Figure 4. Proposed metasurface unit cell. (a) Top View; (b) Perspective view.

Since L_{T1} and L_{T2} in Figure 4 represents the total path transversed by EM waves in the internal and external ring respectively, and the fundamental mode length $\lambda_g/2$ is represented as,

$$L_{T1} = \frac{\lambda_g}{2}, \quad L_{T2} = \frac{\lambda_g}{2}. \quad (1)$$

The guided wavelength at resonant frequency f_o is represented by the following equation [50]

$$\lambda_g = \frac{\lambda_o}{\sqrt{\epsilon_{\text{eff}}}} = \frac{c}{f_o \sqrt{\epsilon_{\text{eff}}}}, \tag{2}$$

therefore, the internal and external ring guided wavelengths λ_{g1} & λ_{g2} respectively are given as

$$\lambda_{g1} = \frac{c}{f_1 \sqrt{\epsilon_{\text{eff}}}}, \quad \lambda_{g2} = \frac{c}{f_2 \sqrt{\epsilon_{\text{eff}}}}, \tag{3}$$

where resonance frequencies of the internal and external rings are defined by f_1 and f_2 respectively. The effective dielectric constant is calculated as [51]

$$\epsilon_{\text{eff}} = \frac{\epsilon_r + 1}{2} + \frac{\epsilon_r - 1}{2} \left[1 + \frac{12h}{W} \right]^{-1/2} \quad \text{for } \frac{W}{h} > 1, \tag{4}$$

where ϵ_r represents the dielectric constant. To attain the internal and external ring average length at any specified resonant frequency, Equation (2) is substituted into Equation (1) to give [50]

$$L_{T1} = \frac{c}{2f_1 \sqrt{\epsilon_{\text{eff}}}}, \quad L_{T2} = \frac{c}{2f_2 \sqrt{\epsilon_{\text{eff}}}}. \tag{5}$$

Furthermore, since the resonators exhibit the same standing waves at the fundamental modes, Equation (5) is used for both one-port and two-port resonators [50].

From the specified substrate information, the dielectric constant ϵ_r and height h are used to calculate the width W of the ring resonator. For a given characteristic impedance Z_o , the width was represented as;

$$W = \begin{cases} \frac{8e^A}{e^{2A}-2} h & \text{for } \frac{W}{h} < 2, \\ \frac{2}{\pi} \left[B - 1 - \ln(2B - 1) + \frac{\epsilon_r - 1}{2\epsilon_r} \left(\ln(B - 1) + 0.39 - \frac{0.61}{\epsilon_r} \right) \right] h & \text{for } \frac{W}{h} > 2, \end{cases} \tag{6}$$

where

$$A = \frac{Z_o}{60} \sqrt{\frac{\epsilon_r + 1}{2}} + \frac{\epsilon_r - 1}{\epsilon_r + 1} \left(0.23 + \frac{0.11}{\epsilon_r} \right), \tag{7}$$

$$B = \frac{377\pi}{2Z_o \sqrt{\epsilon_r}}. \tag{8}$$

From Equation (5), the internal and external side lengths l_1 and l_2 of each ring of the SRR can be calculated by,

$$l_1 = L_{T1} + \frac{W}{2}, \quad l_2 = L_{T2} + \frac{W}{2}. \tag{9}$$

The permittivity and permeability are calculated from the refractive index (η) and impedance values z using Equations (10) and (11) in order to confirm if the designed SRR represents a double negative metamaterial.

$$\epsilon = \frac{\eta}{z}, \tag{10}$$

$$\mu = \eta z, \tag{11}$$

where η and z are denoted as [49,52]

$$\eta = \frac{1}{kl} \Re\{\ln(e^{jnk_{l\text{out}}})\} - \Im\{\ln(e^{jnk_{l\text{out}}})\}, \tag{12}$$

$$z = \frac{(1 + S_{11}^2)^2 - S_{21}^2}{(1 - S_{11}^2)^2 - S_{21}^2}. \tag{13}$$

From Equations (12) and (13), the reflection and transmission coefficients are represented by S_{11}^2 and S_{21}^2 , respectively, $\Re\{\cdot\}$ and $\Im\{\cdot\}$ denote the real and imaginary components, k represents the wave number, and $e^{jnk_{\text{out}}}$ is represented as [53]:

$$e^{jnk_{\text{out}}} = \frac{S_{21}^2}{1 - S_{11} \left(\frac{z-1}{z+1} \right)}. \quad (14)$$

4. Simulation Processes

With the foregoing mathematical analysis, a practical square split ring resonator was designed using CST MWS software. The MWS is based on solving Maxwell's equations in differential form in the time domain explicitly [54]. Additionally, it is highly desirable to use time domain simulations methods for high frequency electromagnetic applications, especially when broadband results are desired [55]. In this work, a square SRR resonating at 28 GHz and 40 GHz was constructed on an RT5880 substrate with a height of 0.5 mm, as depicted in Figure 4. The metallic layer used was the lossy annealed copper. The desired dimensions were obtained by using design equations discussed in Section 3 and a summary of a step-by-step design procedure is shown in Table 1.

Table 1. Summary of calculation of dimensions of a metasurface unit cell.

Step	Equation	Purpose
1	Equation (6)	Calculate the width of a characteristic impedance Z_0
2	Equations (5) and (14)	Calculate the dielectric constant and use it to find the internal and external average lengths L_{T1} & L_{T2} for each frequency
3	Equation (9)	Calculate the internal and external side lengths of each outer ring using the calculated average lengths in Step 2

Following the use of the design procedure, in order to optimize the calculated parameters of the unit cell of the metasurface, the CST optimizer tool from the software was used. Table 2 depicts the dimensions of the unit cell before and after optimization.

Table 2. Unit cell dimensions before and after software optimization.

Dimensions	Before Optimization (mm)	After Optimization (mm)
h	0.5	0.56
W	1.54	1.54
l_1	3.51	3.47
l_2	4.68	4.4

In order to perform simulation in CST MWS, the boundary conditions have to be defined. For the software to generate EM waves, the boundary conditions of the x_{axis} , y_{axis} and z_{axis} were defined as a perfect electric conductor, perfect magnetic conductor and open respectively. This means that for x_{min} and x_{max} the magnetic fluxes are set to zero, for y_{min} and y_{max} electric fluxes are set to zero and with z_{min} and z_{max} waves can pass with minimal reflections. The proposed structure was excited by defining two wave ports which were normal to the x_{axis} . The time domain solver which comprises of finite difference time domain (FDTD) was used to calculate transmission of energy between excitation sources and obtain broadband frequency behaviour of the simulated structure.

To achieve reconfigurability, the designed unit cell was made into a 4×4 element integrated with diodes, as shown in Figure 5. Similar to authors in [56], each unit cell of the metasurface was connected to a diode.

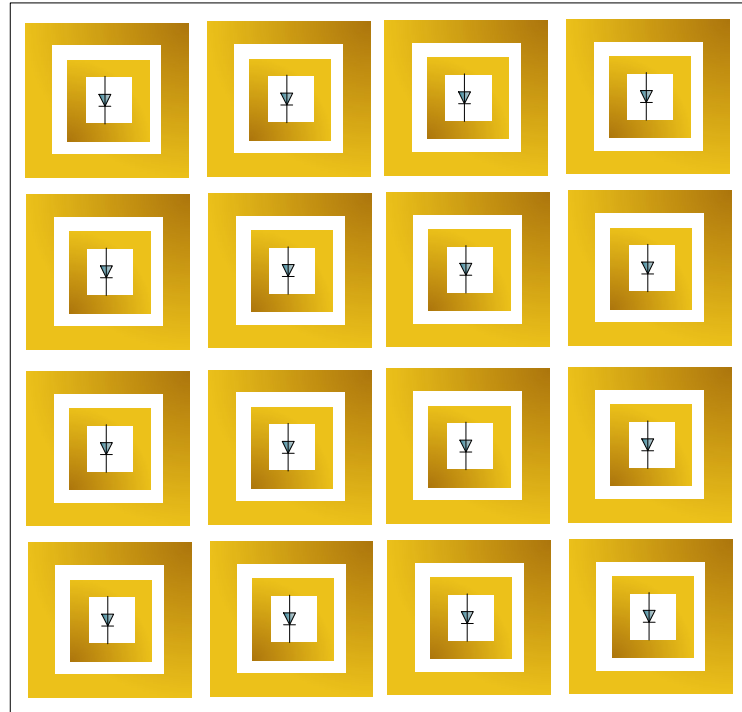


Figure 5. A 4×4 RMS integrated with PIN diodes.

In an array of SRR unit cells, there is an increased magnetic response [57], due to an alternating magnetic field perpendicular to the SRR plane. The SRR behaves as a simple LC resonator, with capacitance resulting from the separation of charges across the split and inductance being the result of currents circulating in the ring, exhibiting a resonant response at a specific frequency [58,59]. The resonant circular currents give rise to a resonant magnetic dipole moment, which is responsible for the negative permeability part of negative refraction [59]. Furthermore, the electromagnetic response can also be influenced by the mutual coupling between SRR unit cells [60]. Mutual coupling is when antenna elements that are near each other, either transmitting or receiving, will leak some of the energy that is intended for one to the other [51]. The strength of coupling between SRR unit cells is dependent on the separation between them and the orientation of each unit cell [59]. In this proposed work, there is high potential existence of mutual coupling since the unit cells are closely spaced by 5.18 mm. In addition, superdirectivity could be achieved due to the proximity of the unit cells from each other [51,61]. However, the focus of this paper is to design a frequency reconfigurable metasurface antenna without mitigating the mutual coupling effect between the unit cells. Mutual coupling effects and superdirectivity will be investigated in future works.

5. Results and Analysis

As a result of the computations from CST MWS, optimized dimensions, return loss curves, reflection phase, gain, directivity, effective permittivity, and permeability of the proposed frequency RMS were analyzed in this section.

5.1. Reflection Coefficient

For resonant frequencies of 28 GHz and 40 GHz, a reflection coefficient/return loss graph that shows the ratio of the amplitude of the reflected wave to the incident wave was simulated, yielding the results shown in Figure 6. As seen from the figure, before

optimization, the unit cell resonated at 25.6 GHz and 39.85 GHz with a magnitude of -14.80 dB and -13.11 dB, respectively. With the use of the CST optimizer, the unit cell resonated at 28.3 GHz and 40.3 GHz with a reflection coefficient of -18.57 dB and -22.0 dB, respectively. The bandwidth of the unit cell before optimization was 4.65 GHz and 0.67 GHz and, after optimization, as depicted at the -10 dB mark in Figure 6, it was 6.8 GHz and 1.50 GHz. When the unit cell was optimized, it resonated at a frequency closer to the desired operating frequencies (i.e., 28 GHz and 40 GHz) with less reflection than before. As a result, the optimized return loss results of the unit cell were used to analyze a 4×4 frequency RMS antenna structure shown in Figure 5. The student version simulation software was not licensed for hundreds of elements, therefore an array characterized by 16 elements was chosen.

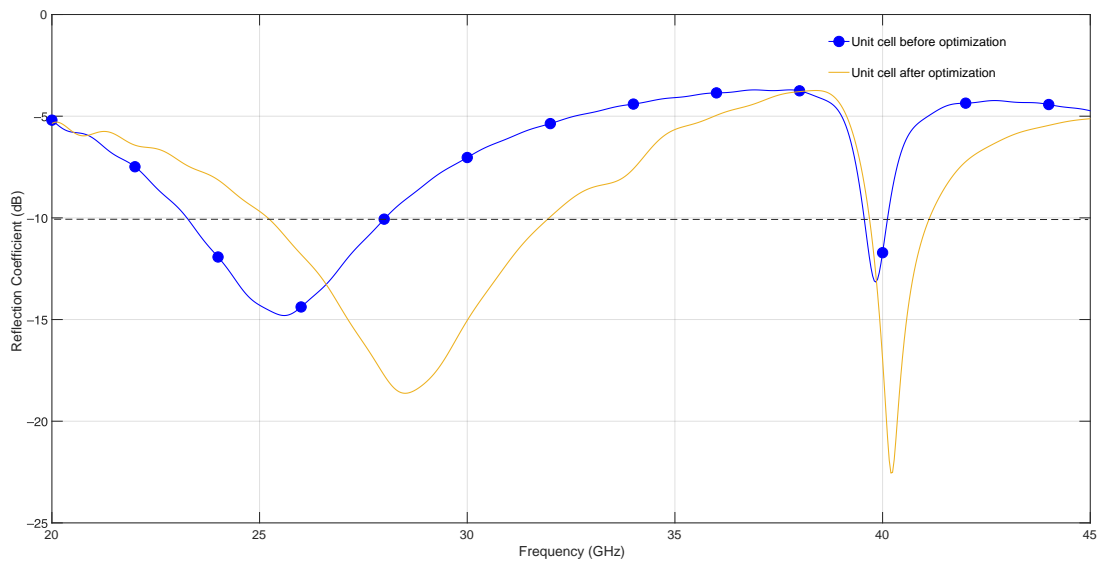


Figure 6. Return loss results of metasurface unit cell before and after optimization.

Figure 7 depicts the return loss results for a 4×4 metasurface antenna with and without adding PIN diodes from the lumped elements section in CST MWS, which enable frequency reconfigurability. The results are further numerically summarized in Table 3. It was observed that when diodes were added, the resonating frequency decreased as the capacitance increased. From the table, the bandwidth of the 16 element metasurface antenna without diodes was relatively the same as when they were added. Furthermore, it can be observed from this table and figure that the proposed metasurface antenna array was capable of frequency reconfiguration.

Table 3. Summary of return loss and bandwidth results.

Capacitance (pF)	Resonating Frequency (GHz)	Bandwidth (GHz)
Without diodes	26.90–31.39, 32.26, and 40.20	4.46, 0.66, and 1.36
0.03	26.61–31.49, 32.49, and 40.28	4.88, 0.42, and 1.41
0.035	23.60, 26.72–31.47, 32.48, and 40.28	1.17, 4.73, 0.43, and 1.41
0.04	23.08, 26.79–31.46, 32.48, and 40.24	1.17, 4.68, 0.44, and 1.39
0.045	22.72, 26.81–31.44, 32.48, and 40.24	1.05, 4.63, 0.45, and 1.38
0.05	22.48, 26.89–31.43, 32.44, and 40.24	0.98, 4.58, 0.46, and 1.38

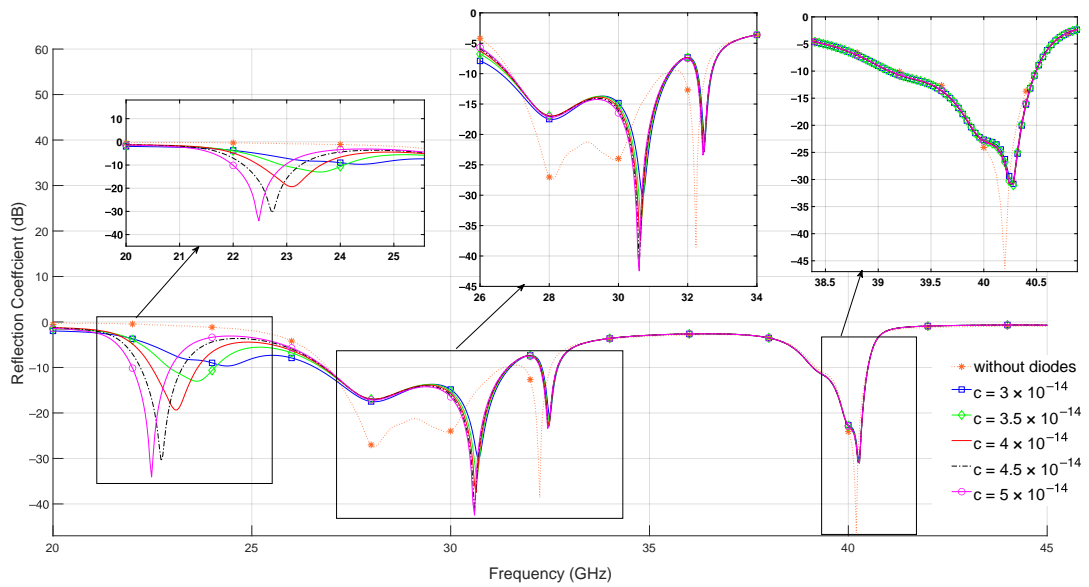


Figure 7. Return loss simulation results of 16 element metasurface array with and without PIN diodes.

5.2. Reflection Phase

Figure 8 shows the reflection phase for the proposed 16 elements metasurface antenna with and without PIN diodes. As observed from the figure, there was a phase difference of 21.8° and 4.3° at 28 GHz and 40 GHz (designed operating frequencies), respectively, as diode capacitance was increased. Additionally, before adding the diodes, there was a phase shift of 360° at 26.08 GHz and at 26.68 GHz when the diodes were added for all capacitance values. The same phase shift was also observed at 22.7 GHz for when capacitance was 0.05 pF.

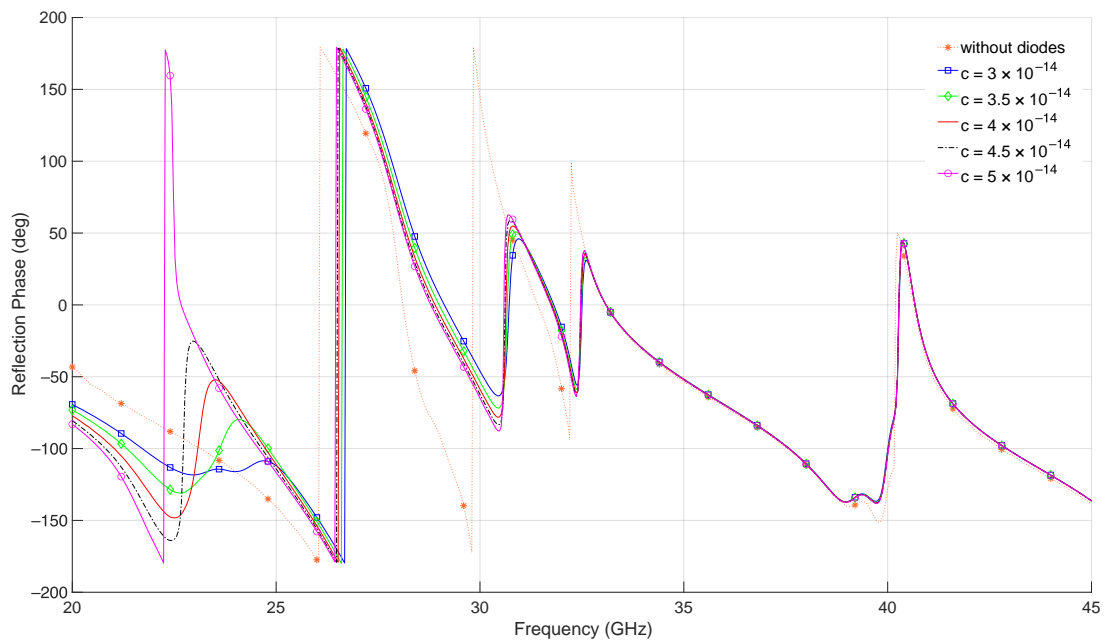


Figure 8. Reflection phase of the 16 element metasurface array with and without PIN diodes.

Figure 8 further shows that for a frequency reconfigurable metasurface, the capacitance increases when the operating frequency decreases [62,63].

5.3. Gain and Directivity

According to [51], directivity is a property of RF systems which determines how concentrated the radiation emitted is in one direction. It is a factor affecting the gain in these systems. The gain describes how well the proposed structure converts input power into radio waves, which travel in a particular direction [51]. Despite the fact that the gain of the metasurface antenna is closely related to its directivity, it is also a measure of its efficiency and directional capabilities [51]. The simulated results in Figure 9 depict the directivity and gain results before and after the lumped elements were installed on the 16 element metasurface antenna. Table 4 shows a numerical summary of the figure.

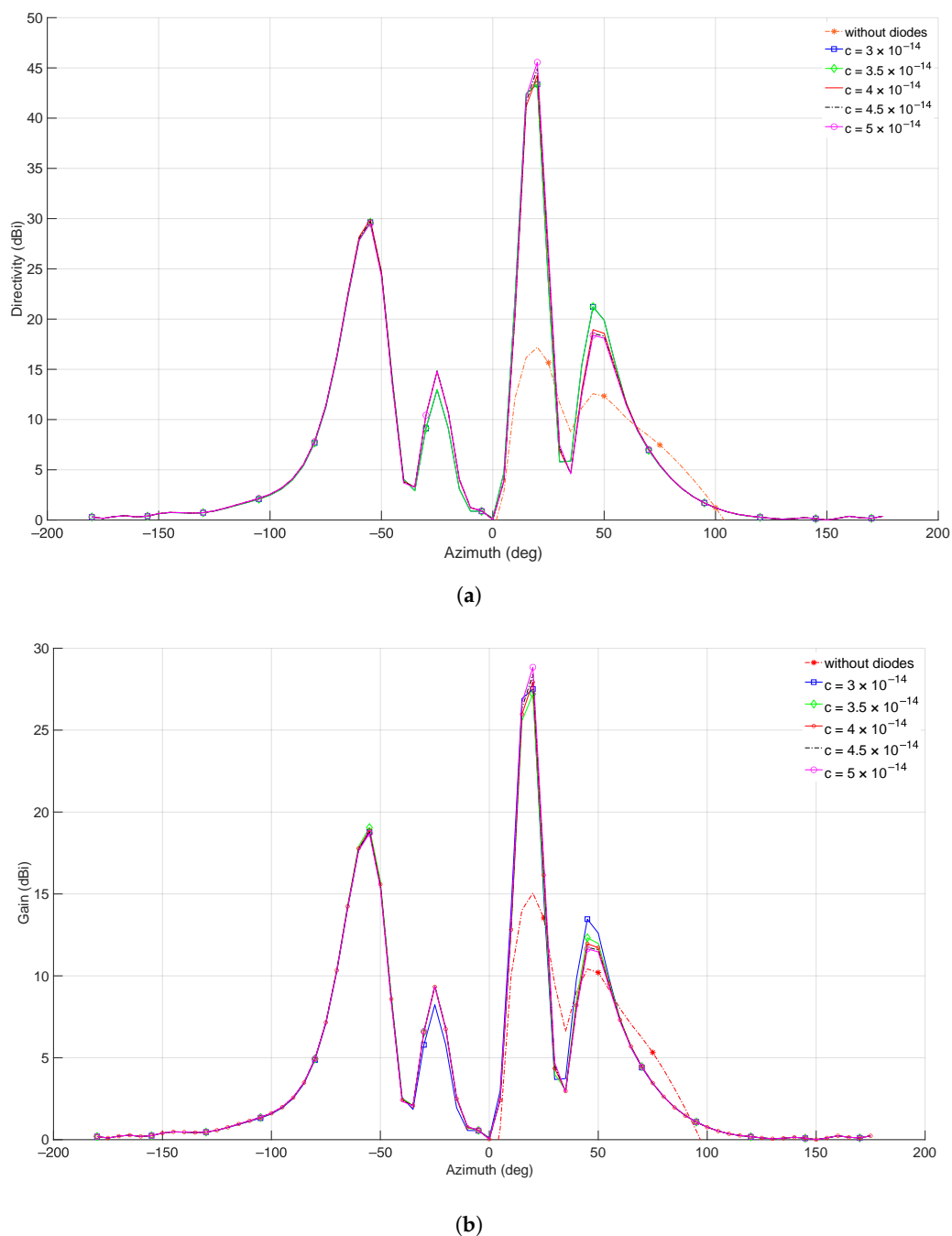


Figure 9. Simulation results of a 16 element metasurface array with and without PIN diodes indicating (a) Directivity (b) Gain.

From Table 4, the gain and directivity of the reconfigurable 16 elements metasurface antenna increased when diodes were added. This is due to the decreased angular beamwidth, which led to a narrower beam, resulting in higher directivity and gain [64]. However, since the proposed SRR unit cells are made of copper, when the current is applied, it moves towards the surface of the conducting material, decreasing its effective cross section. This tendency is known as the skin effect and it is the reason attenuation increases with frequency because of high loss resistance. This can result in decreased gain and should be taken into consideration during the design and implementation processes. Furthermore, the directivity and gain were used to compute the radiation efficiency using Equation (15) [51,65]

$$\text{Radiation efficiency} = \frac{\text{Gain (dBi)}}{\text{Directivity (dBi)}} \times 100\%. \quad (15)$$

Since PIN diodes are connected to metallic strips of the metasurface antenna array, loss can occur due to the dissipation of power, which affects the radiation efficiency. It was observed from Table 4 that the radiation efficiency of the metasurface antenna array decreased when diodes were added.

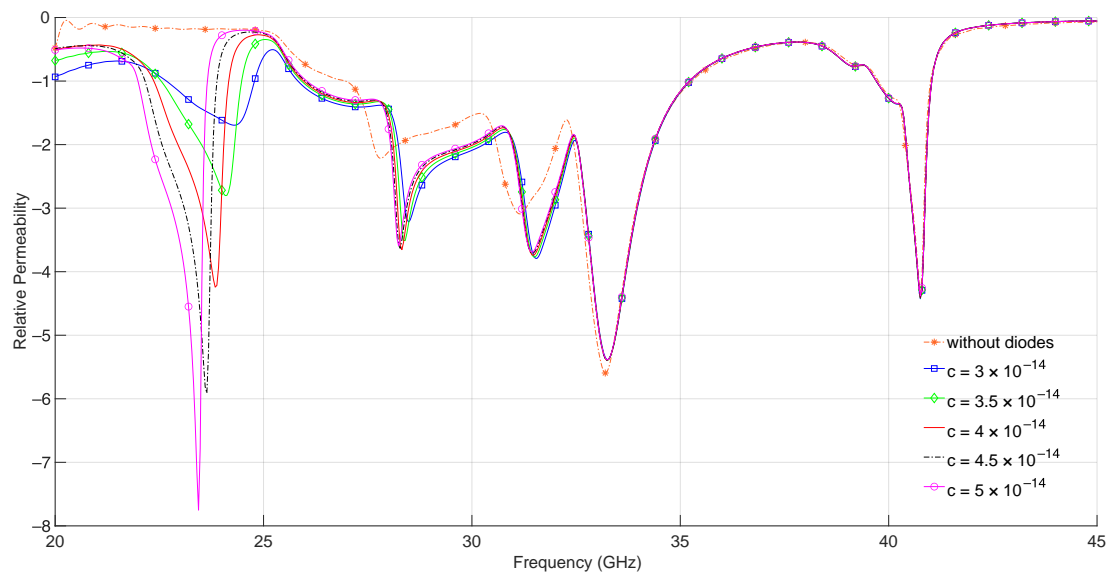
Table 4. Summary of the gain, directivity, and radiation efficiency.

Capacitance (pF)	Angular Beamwidth (°)	Gain (dBi)	Directivity (dBi)	Radiation Efficiency (%)
Without diodes	16.5	15	17.2	87.2
0.03	15.3	27.23	43.37	62.79
0.035	15.0	27.50	43.06	63.86
0.04	14.5	27.93	44.28	63.08
0.045	14.31	28.42	44.93	63.25
0.05	13.9	28.8	45.6	63.31

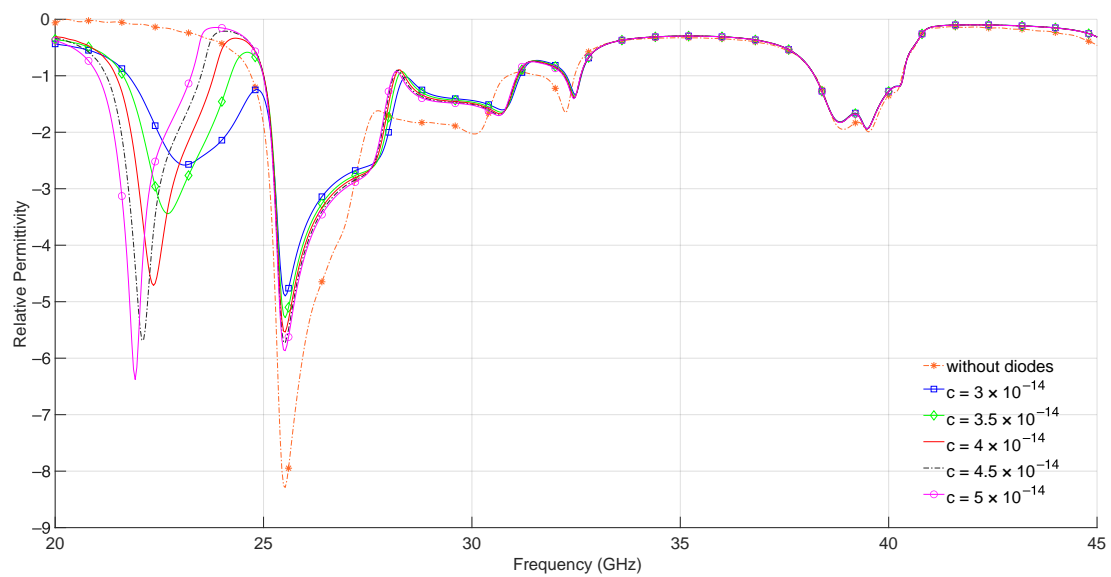
According to [66], the resistance of the diode does not affect the operating frequency. As a result, capacitance and inductance of the switches have no effect on the gain nor directivity. From Table 4, the directivity, gain, and radiation efficiency with varying capacitances was relatively the same.

5.4. Effective Permittivity, and Permeability

From Figure 10, the 16 elements metasurface antenna permittivity and permeability before and after adding diodes were all negative. These results were obtained from the CST MWS software, which used a method by [67] to retrieve the effective constitutive parameters (permittivity and permeability) of a slab of metamaterial from the measurement of scattering parameters. Frequency reconfigurability can also be observed from this figure. Since μ and ϵ were negative at all resonating frequencies, as shown in Figure 10a,b, this indicates that both the designed 4×4 metasurface antenna structure and its frequency reconfigurable structure were double negative metasurfaces, which exhibits the phenomenal ability of negative refraction. Furthermore, Equations (10) and (11) can be used to verify whether μ and ϵ are negative.



(a)



(b)

Figure 10. Retrieved effective constitutive parameters of the simulated results (a) Effective permeability (b) Effective permittivity.

5.5. Comparison with Previous Work

The performance comparisons between the proposed 16 elements frequency RMS antenna and other designs are given in Table 5.

It can be observed from this table that previous work did not specify how the dimensions of the metasurface were calculated.

Table 5. Comparisons between proposed 16 elements frequency RMS and existing designs.

Ref	Size (mm ²)	Reconfiguration	Actuators	Frequency Band	Detailed Design Procedure
[68]	2 × 4	Frequency	GaAs air-bridged Schottky diode	mmWave	Not specified
[42]	80 × 80	Pattern	12 PIN diodes	Sub-mmWave	Not specified
[43]	180 × 180	Frequency	Liquid metal	Sub-mmWave	Not specified
[44]	117 × 117	Frequency and Pattern	16 PIN diodes	mmWave	Not specified
This work	17.6 × 17.6	Frequency	16 PIN diodes	mmWave	Specified

6. Conclusions

This work proposed a step-by-step design method for a frequency reconfigurable metasurface antenna with the ability to adjust its operating frequency by utilizing semiconductor diodes such as PIN diodes. A simplified unified demonstration on how a metasurface antenna unit cell was designed theoretically from split ring resonators in order to attain its geometrical dimensions at any frequency of resonance was shown. The radiation mechanisms of the 16 element metasurface and RMS antenna were explained in detail via the reflection phase and its magnitude characteristics. It was observed that when diodes were added, the resonating frequency decreased as the capacitance increased. The proposed frequency RMS antenna exhibited a wideband operational bandwidth from 25 to 32 GHz and approximately at 40 GHz. In addition, multiple gain variations from 27.33 dBi to 28.8 dBi were observed across the full operating band at different diode capacitances. It was also observed that the gain and directivity increased when diodes were added due to decreased angular beamwidth. However, radiation efficiency decreased because of the loss that occurred due to the dissipation of power from the added diodes. From the proposed frequency RMS antenna, the gain, directivity, and radiation efficiency did not vary as the frequency of operation changed. The proposed 16 elements structure has proven to be a double negative metasurface, which means that it has the ability to dynamically shape electromagnetic fields. There has been considerable success with reconfigurable metasurface antennas in the microwave regime, but the use of metasurfaces in future communication has enormous potential for further research.

Author Contributions: Methodology, B.K.L.; supervision, M.M. and B.B.; writing—review and editing, P.M. and R.R. All authors have read and agreed to the published version of the manuscript.

Funding: This research was funded by Botswana International University of Science and Technology grant number S00190 and S00378.

Conflicts of Interest: The authors declare no conflict of interest.

References

- Masoudi, M.; Khafagy, M.G.; Conte, A.; El-Amine, A.; Françoise, B.; Nadjahi, C.; Salem, F.E.; Labidi, W.; Süral, A.; Gati, A.; et al. Green Mobile Networks for 5G and Beyond. *IEEE Access* **2019**, *7*, 107270–107299. [[CrossRef](#)]
- Meng, X.; Nekovee, M.; Wu, D. Reconfigurable liquid crystal reflectarray metasurface for THz communications. In Proceedings of the Antennas and Propagation Conference 2019 (APC-2019), Birmingham, UK, 11–12 November 2019; pp. 1–6. [[CrossRef](#)]
- Yang, P.; Xiao, Y.; Xiao, M.; Li, S. 6G Wireless Communications: Vision and Potential Techniques. *IEEE Netw.* **2019**, *33*, 70–75. [[CrossRef](#)]
- Awan, W.A.; Alibakhshikenari, M.; Limiti, E. Design and Analysis of a Simple Miniaturized Fractal Antenna for 5G Ka-Band Applications. In Proceedings of the 2021 IEEE Asia-Pacific Microwave Conference (APMC), Brisbane, Australia, 28 November–1 December 2021; pp. 22–24. [[CrossRef](#)]
- Naqvi, S.A.; Awan, W.A.; Alibakhshikenari, M.; Falcone, F.; Limiti, E. Design and Characterization of a Simple and Wideband Antenna for 5G mm-wave Applications. In Proceedings of the 2020 IEEE MTT-S Latin America Microwave Conference (LAMC 2020), Cali, Colombia, 26–28 May 2021; pp. 1–3. [[CrossRef](#)]
- Rusek, F.; Persson, D.; Lau, B.K.; Larsson, E.G.; Marzetta, T.L.; Edfors, O.; Tufvesson, F. Scaling up MIMO: Opportunities and challenges with very large arrays. *IEEE Signal Process. Mag.* **2012**, *30*, 40–60. [[CrossRef](#)]

7. Chataut, R.; Akl, R. Massive MIMO Systems for 5G and beyond Networks—Overview, Recent Trends, Challenges, and Future Research Direction. *Sensors* **2020**, *20*, 2753. [[CrossRef](#)]
8. Shlezinger, N.; Dicker, O.; Eldar, Y.C.; Yoo, I.; Imani, M.F.; Smith, D.R. Dynamic Metasurface Antennas for Uplink Massive MIMO Systems. *IEEE Trans. Commun.* **2019**, *67*, 6829–6843. [[CrossRef](#)]
9. Alkhateeb, A.; Mo, J.; González-Prelcic, N.; Heath, R. MIMO precoding and combining solutions for millimeter-wave systems. *IEEE Commun. Soc. Mag.* **2014**, *52*, 122–131. [[CrossRef](#)]
10. Mo, J.; Alkhateeb, A.; Abu-Surra, S.; Heath, R.W. Hybrid Architectures with Few-Bit ADC Receivers: Achievable Rates and Energy-Rate Tradeoffs. *IEEE Trans. Wirel. Commun.* **2017**, *16*, 2274–2287. [[CrossRef](#)]
11. Sleasman, T.; Boyarsky, M.; Pulido-Mancera, L.; Fromenteze, T.; Imani, M.F.; Reynolds, M.S.; Smith, D.R. Experimental Synthetic Aperture Radar with Dynamic Metasurfaces. *IEEE Trans. Antennas Propag.* **2017**, *65*, 6864–6877. [[CrossRef](#)]
12. Yang, W.; Chen, S.; Che, W.; Xue, Q.; Meng, Q. Compact High-Gain Metasurface Antenna Arrays Based on Higher-Mode SIW Cavities. *IEEE Trans. Antennas Propag.* **2018**, *66*, 4918–4923. [[CrossRef](#)]
13. Smith, D.R.; Yurduseven, O.; Mancera, L.P.; Bowen, P.; Kundtz, N.B. Analysis of a Waveguide-Fed Metasurface Antenna. *Phys. Rev. Appl.* **2017**, *8*, 054048. [[CrossRef](#)]
14. Yoo, I.; Imani, M.F.; Sleasman, T.; Pfister, H.D.; Smith, D.R. Enhancing Capacity of Spatial Multiplexing Systems Using Reconfigurable Cavity-Backed Metasurface Antennas in Clustered MIMO Channels. *IEEE Trans. Commun.* **2019**, *67*, 1070–1084. [[CrossRef](#)]
15. Rotshild, D.; Rahamim, E.; Abramovich, A. Innovative Reconfigurable Metasurface 2-D Beam-Steerable Reflector for 5G Wireless Communication. *Electronics* **2020**, *9*, 1191. [[CrossRef](#)]
16. Achouri, K.; Salem, M.A.; Caloz, C. General Metasurface Synthesis Based on Susceptibility Tensors. *IEEE Trans. Antennas Propag.* **2015**, *63*, 2977–2991. [[CrossRef](#)]
17. Vahabzadeh, Y.; Chamanara, N.; Achouri, K.; Caloz, C. Computational analysis of metasurfaces. *IEEE J. Multiscale Multiphys. Comput. Tech.* **2018**, *3*, 37–49. [[CrossRef](#)]
18. Chen, H.T.; Taylor, A.J.; Yu, N. A review of metasurfaces: Physics and applications. *Rep. Prog. Phys.* **2016**, *79*, 76401. [[CrossRef](#)]
19. Bukhari, S.S.; Vardaxoglou, J.; Whittow, W. A Metasurfaces Review: Definitions and Applications. *Appl. Sci.* **2019**, *9*, 2727. [[CrossRef](#)]
20. Choudhury, P.; El-Nasr, M.A. Waves in resonant metasurfaces. *J. Electromagn. Waves Appl.* **2020**, *34*, 1309–1313. [[CrossRef](#)]
21. Yu, N.; Capasso, F. Flat optics with designer metasurfaces. *Nat. Mater.* **2014**, *13*, 139–150. [[CrossRef](#)]
22. He, Q.; Sun, S.; Zhou, L. Tunable/Reconfigurable Metasurfaces: Physics and Applications. *Research* **2019**, *2019*, 1849272. [[CrossRef](#)]
23. Zheludev, N.; Kivshar, Y. From metamaterials to metadevices. *Nat. Mater.* **2012**, *11*, 917–924. [[CrossRef](#)]
24. Veselago, V.G. The Electrodynamics of substances with simultaneously negative values of ϵ and μ . *Usp. Fiz. Nauk* **1967**, *92*, 517. [[CrossRef](#)]
25. Krzysztofik, W.J.; Cao, T.N. Metamaterials in application to improve antenna parameters. *Metamater. Metasurf.* **2018**, *12*, 63–85.
26. Antipov, S.; Liu, W.; Power, J.; Spentzouris, L. Left-Handed Metamaterials Studies and their Application to Accelerator Physics. In Proceedings of the 2005 Particle Accelerator Conference, Knoxville, TN, USA, 16–20 May 2005; pp. 458–460. [[CrossRef](#)]
27. Tong, X.C. *Functional Metamaterials and Metadevices*; Springer: Cham, Switzerland, 2018.
28. Alici, K.B.; Ozbay, E. Radiation properties of a split ring resonator and monopole composite. *Phys. Status Solidi B Basic Solid State Phys.* **2007**, *244*, 1192–1196. [[CrossRef](#)]
29. Sliusar, I.; Slyusar, V.; Utkin, Y.; Kopishynska, O. Parametric synthesis of 3D structure of SRR element of the metamaterial. In Proceedings of the 2020 IEEE International Conference on Problems of Infocommunications. Science and Technology (PIC S&T), Kharkiv, Ukraine, 6–9 October 2020; pp. 577–582.
30. Aydin, K.; Guven, K.; Kafesaki, M.; Soukoulis, C.; Ozbay, E. Experimental observation of true left-handed transmission peak in metamaterials. *Opt. Lett.* **2004**, *29*, 2623–2625. [[CrossRef](#)]
31. Shaltout, A.; Kinsey, N.; Kim, J.; Chandrasekar, R.; Ndukaife, J.; Boltasseva, A.; Shalae, V. Development of Optical Metasurfaces: Emerging Concepts and New Materials. *Proc. IEEE* **2016**, *104*, 1–18. [[CrossRef](#)]
32. Basar, E. Transmission through Large Intelligent Surfaces: A New Frontier in Wireless Communications. In Proceedings of the 2019 European Conference on Networks and Communications (EuCNC), Valencia, Spain, 18–21 June 2019; pp. 112–117. [[CrossRef](#)]
33. Lv, L.; Wu, Q.; Li, Z.; Al-Dhahir, N.; Chen, J. Secure Two-Way Communications via Intelligent Reflecting Surfaces. *IEEE Commun. Lett.* **2021**, *25*, 744–748. [[CrossRef](#)]
34. Wu, Q.; Zhang, R. Intelligent Reflecting Surface Enhanced Wireless Network via Joint Active and Passive Beamforming. *IEEE Trans. Wirel. Commun.* **2019**, *18*, 5394–5409. [[CrossRef](#)]
35. Feng, K.; Li, X.; Han, Y.; Jin, S.; Chen, Y. Physical Layer Security Enhancement Exploiting Intelligent Reflecting Surface. *IEEE Commun. Lett.* **2021**, *25*, 734–738. [[CrossRef](#)]
36. Shlezinger, N.; Alexandropoulos, G.C.; Imani, M.F.; Eldar, Y.C.; Smith, D.R. Dynamic metasurface antennas for 6G extreme massive MIMO communications. *IEEE Wirel. Commun.* **2021**, *28*, 106–113. [[CrossRef](#)]
37. Guanxing, Z.; Liu, Z.; Deng, W.; Zhu, W. Reconfigurable metasurfaces with mechanical actuations: Towards flexible and tunable photonic devices. *J. Opt.* **2020**, *23*, 013001. [[CrossRef](#)]

38. Tang, W.; Dai, J.Y.; Chen, M.; Li, X.; Cheng, Q.; Jin, S.; Wong, K.K.; Cui, T.J. Programmable metasurface-based RF chain-free 8PSK wireless transmitter. *Electron. Lett.* **2019**, *55*, 417–420. [[CrossRef](#)]
39. Tsilipakos, O.; Tasolamprou, A.; Pitolakis, A.; Liu, F.; Wang, X.; Mirmoosa, M.; Tzarouchis, D.; Abadal, S.; Taghvaei, H.; Liaskos, C.; et al. Toward intelligent metasurfaces: The progress from globally tunable metasurfaces to software-defined metasurfaces with an embedded network of controllers. *Adv. Opt. Mater.* **2020**, *8*, 2000783. [[CrossRef](#)]
40. Liu, F.; Tsilipakos, O.; Pitolakis, A.; Tasolamprou, A.; Mirmoosa, M.; Kantartzis, N.; Kwon, D.; Kafesaki, M.; Soukoulis, C.; Tretyakov, S. Intelligent Metasurfaces with Continuously Tunable Local Surface Impedance for Multiple Reconfigurable Functions. *Phys. Rev. Appl.* **2019**, *11*, 044024. [[CrossRef](#)]
41. Huang, C.; Zhang, C.; Yang, J.; Sun, B.; Zhao, B.; Luo, X. Reconfigurable Metasurface for Multifunctional Control of Electromagnetic Waves. *Adv. Opt. Mater.* **2017**, *5*, 1700485. [[CrossRef](#)]
42. Chaimool, S.; Hongnara, T.; Rakluea, C.; Akkaraekthalin, P.; Zhao, Y. Design of a PIN Diode-Based Reconfigurable Metasurface Antenna for Beam Switching Applications. *Int. J. Antennas Propag.* **2019**, *2019*, 7216324. [[CrossRef](#)]
43. Qian, T. Reconfigurable Metasurface Antenna Based on the Liquid Metal for Flexible Scattering Fields Manipulation. *Micromachines* **2021**, *12*, 243. [[CrossRef](#)]
44. Li, W.; Wang, Y.M.; Hei, Y.; Li, B.; Shi, X. A Compact Low-Profile Reconfigurable Metasurface Antenna with Polarization and Pattern Diversities. *IEEE Antennas Wirel. Propag. Lett.* **2021**, *20*, 1170–1174. [[CrossRef](#)]
45. Nemati, A.; Wang, Q.; Hong, M.; Teng, J. Tunable and reconfigurable metasurfaces and metadevices. *Opto-Electron. Adv.* **2018**, *1*, 180009. [[CrossRef](#)]
46. Yurduseven, O.; Smith, D.R.; Fromenteze, T. Design of a Reconfigurable Metasurface Antenna for Dynamic Near-Field Focusing. In Proceedings of the 2018 IEEE International Symposium on Antennas and Propagation USNC/URSI National Radio Science Meeting, Boston, MA, USA, 8–13 July 2018; pp. 1707–1708. [[CrossRef](#)]
47. Chen, L.; Ruan, Y.; Cui, H.Y. Liquid metal metasurface for flexible beam-steering. *Opt. Express* **2019**, *27*, 23282–23292. [[CrossRef](#)]
48. Abdalrazik, A.; Abdel-Rahman, A.B.; Allam, A.; Abo-Zahhad, M.; Yoshitomi, K.; Pokharel, R.K. Frequency-reconfigurable dielectric resonator antenna using metasurface. *Int. J. Microw. Wirel. Technol.* **2021**, 1–7. [[CrossRef](#)]
49. Xavier, G.; Serres, A.; Costa, E.; Oliveira, A.; Nobrega, L.; Souza, V. Design and Application of a Metamaterial Superstrate on a Bio-Inspired Antenna for Partial Discharge Detection through Dielectric Windows. *Sensors* **2019**, *19*, 4255. [[CrossRef](#)] [[PubMed](#)]
50. Chang, K.; Hsieh, L.H. *Microwave Ring Circuits and Related Structures*; Wiley Online Library: Hoboken, NJ, USA, 2004; Volume 156.
51. Balanis, C.A. *Antenna Theory: Analysis and Design*, 4th ed.; Wiley: Hoboken, NJ, USA, 2015; p. 1104.
52. Kumar, M.S.; Basarkod, P.I. A Study of the Effect of Dielectric Composition on Metamaterial Performance in a Multilayer Environment. In Proceedings of the 2019 International Conference on Data Science and Communication (IconDSC), Bangalore, India, 1–2 March 2019; pp. 1–5. [[CrossRef](#)]
53. Smith, D.R.; Schultz, S.; Marko, P.; Soukoulis, C. Determination of effective permittivity and permeability of metamaterials from reflection and transmission coefficients. *Phys. Rev. B* **2002**, *65*, 195104. [[CrossRef](#)]
54. Pujari, P.; Vyras, K.; Sharma, B.K. Design & Simulation of Circular Patch Antenna for Multiband application of X Band Using Varactor Diodes. In Proceedings of the Conference on Advances in Communication and Control Systems (CAC2S 2013), Dehradun, India, 6–8 April 2013; Atlantis Press: Paris, France, April 2013; pp. 140–144.
55. Barrowes, B.; Prishvin, M.; Jutras, G.; Shubitidze, F. High-Frequency Electromagnetic Induction (HFEMI) Sensor Results from IED Constituent Parts. *Remote Sens.* **2019**, *11*, 2355. [[CrossRef](#)]
56. Yang, H.; Cao, X.; Yang, F.; Gao, J.; Xu, S.; Li, M.; Chen, X.; Zhao, Y.; Zheng, Y.; Li, S. A programmable metasurface with dynamic polarization, scattering and focusing control. *Sci. Rep.* **2016**, *6*, 35692. [[CrossRef](#)] [[PubMed](#)]
57. Feth, N.; König, M.; Husnik, M.; Stannigel, K.; Niegemann, J.; Busch, K.; Wegener, M.; Linden, S. Electromagnetic interaction of split-ring resonators: The role of separation and relative orientation. *Opt. Express* **2010**, *18*, 6545–6554. [[CrossRef](#)] [[PubMed](#)]
58. Penciu, R.S.; Aydin, K.; Kafesaki, M.; Koschny, T.; Ozbay, E.; Economou, E.N.; Soukoulis, C.M. Multi-gap individual and coupled split-ring resonator structures. *Opt. Express* **2008**, *16*, 18131–18144. [[CrossRef](#)] [[PubMed](#)]
59. Seetharaman, S.S.; King, C.; Hooper, I.R.; Barnes, W.L. Electromagnetic interactions in a pair of coupled split-ring resonators. *Phys. Rev. B* **2017**, *96*, 085426. [[CrossRef](#)]
60. Tatartschuk, E.; Gneiding, N.; Hesmer, F.; Radkovskaya, A.A.; Shamonina, E. Mapping inter-element coupling in metamaterials: Scaling down to infrared. *J. Appl. Phys.* **2012**, *111*, 094904. [[CrossRef](#)]
61. Radkovskaya, A.; Kiriushchekina, S.; Vakulenko, A.; Petrov, P.; Solymar, L.; Li, L.; Vallecchi, A.; Stevens, C.; Shamonina, E. Superdirectivity from arrays of strongly coupled meta-atoms. *J. Appl. Phys.* **2018**, *124*, 104901. [[CrossRef](#)]
62. Sydoruk, O.; Tatartschuk, E.; Shamonina, E.; Solymar, L. Analytical formulation for the resonant frequency of split rings. *J. Appl. Phys.* **2009**, *105*, 014903. [[CrossRef](#)]
63. Ashoor, A.; Gupta, S. Metasurface Reflector with Real-Time Independent Magnitude and Phase Control. *arXiv* **2020**, arXiv:2009.13369.
64. Poisel, R. *Antenna Systems and Electronic Warfare Applications*; Artech House: Sydney, Australia, 2012.
65. Nassar, I.T.; Weller, T.M. An electrically small meandered line antenna with truncated ground plane. In Proceedings of the 2011 IEEE Radio and Wireless Symposium, Phoenix, AZ, USA, 16–19 January 2011; pp. 94–97.

66. Shirazi, M.; Li, T.; Gong, X. Effects of PIN diode switches on the performance of reconfigurable slot-ring antenna. In Proceedings of the 2015 IEEE 16th Annual Wireless and Microwave Technology Conference (WAMICON), Cocoa Beach, FL, USA, 13–15 April 2015; pp. 1–3.
67. Chen, X.; Grzegorzczak, T.; Wu, B.I.; Pacheco, J.; Kong, J. Robust method to retrieve the constitutive effective parameters of metamaterials. *Phys. Rev. E Stat. Nonlinear Soft Matter Phys.* **2004**, *70 Pt 2*, 016608. [[CrossRef](#)] [[PubMed](#)]
68. Vassos, E.; Churm, J.; Powell, J.; Viegas, C.; Alderman, B.; Feresidis, A. Air-bridged Schottky diodes for dynamically tunable millimeter-wave metamaterial phase shifters. *Sci. Rep.* **2021**, *11*, 5988. [[CrossRef](#)] [[PubMed](#)]